Wideband low-noise optical beam deflection sensor with photothermal excitation for liquid-environment atomic force microscopy

doi: 10.1063/1.3086418

Wideband low-noise optical beam deflection sensor with photothermal excitation for liquid-environment atomic force microscopy

Takeshi Fukuma[1,2,a)]
[1]*Frontier Science Organization, Kanazawa University, Kakuma-machi, 920-1192 Kanazawa, Japan*
[2]*PRESTO, Japan Science and Technology Agency, Honcho 4-1-9, Kawaguchi, Japan*

(Received 7 October 2008; accepted 1 February 2009; published online 24 February 2009)

I developed a wideband low-noise optical beam deflection sensor with a photothermal cantilever excitation system for liquid-environment atomic force microscopy. The developed sensor has a 10 MHz bandwidth and 4.7 fm/$\sqrt{\text{Hz}}$ deflection noise density in water. The theoretically limited noise performance (i.e., the noise level limited only by the photodiode shot noise) has been achieved in liquid for the first time. Owing to the wide bandwidth and the replaceable focus lens design, the sensor is applicable to cantilevers with various dimensions. The deflection noise densities of less than 7.8 fm/$\sqrt{\text{Hz}}$ have been achieved in water for cantilevers with lengths from 35 to 125 μm. The ideal amplitude and phase versus frequency curves without distortion are obtained with the developed photothermal excitation system. The excitation system is applicable to relatively stiff cantilevers (>20 N/m) in liquid, making it possible to obtain true atomic-resolution images in liquid. True atomic-resolution imaging of mica in water is demonstrated using the developed deflection sensor and the photothermal excitation system. © *2009 American Institute of Physics.* [DOI: 10.1063/1.3086418]

I. INTRODUCTION

The cantilever deflection sensor is one of the most important elements of the atomic force microscope (AFM).[1] The bandwidth of the sensor determines the frequency range of the cantilever resonance (f_0) available in the AFM experiments. The noise from the deflection sensor can limit the force sensitivity in AFM imaging and spectroscopy. The noise performance can also influence the stability of the cantilever self-oscillation in frequency modulation AFM (FM-AFM).[2]

Among the methods proposed for detecting cantilever deflection,[1,3–9] the optical beam deflection (OBD) method[5] has been the most widely used owing to the simple experimental setup and easy optical beam alignment. Until recently, however, the noise performance of the OBD sensors has been inferior to that of the interferometers. The power spectral density (PSD) of the deflection noise arising from the deflection sensor (n_{zs}) was typically 100–1000 fm/$\sqrt{\text{Hz}}$ for an OBD sensor,[10] while that for an interferometer was typically 10–100 fm/$\sqrt{\text{Hz}}$.

The situation was dramatically changed in 2005. The OBD sensor with n_{zs} of 17 fm/$\sqrt{\text{Hz}}$ in air and 40 fm/$\sqrt{\text{Hz}}$ in water was developed by introducing the radio-frequency (rf) laser power modulation technique and refining the optical design.[11] The reduction of n_{zs} enabled the oscillation of a stiff cantilever ($k>20$ N/m) with small oscillation amplitude ($A<0.5$ nm) and thereby true atomic resolution FM-AFM in liquid.[12] These results highlighted the grave impact of n_{zs} on AFM performance.

In 2006, an OBD sensor with improved n_{zs} values of 5.7 fm/$\sqrt{\text{Hz}}$ in air and 7.3 fm/$\sqrt{\text{Hz}}$ in water was developed using a small diameter laser beam source and replaceable objective lenses.[13] Combined with a liquid-environment FM-AFM, the OBD sensor made it possible to visualize hydration layers[14] and mobile ions[15] at the interface between a model biological membrane and physiological solution with Ångstrom resolution. The biomolecular assemblies, amyloid fibrils, are also imaged in liquid, showing the arrangements of individual β-strands at Ångstrom resolution.[16] These results demonstrated the applicability of low-noise FM-AFM to molecular-scale investigations of biological systems.

After those previous works, the present study is aimed at resolving the remaining design issues. First, the n_{zs} value of the OBD sensor should ultimately be limited by the photodiode shot noise.[11] However, the OBD sensors reported so far have not reached the shot-noise-limited performance in liquid,[13] although it has been possible in air.[11,13] Second, the low-noise (i.e., $n_{zs}<50$ fm/$\sqrt{\text{Hz}}$ in liquid) OBD sensors reported so far have the detection bandwidth (B) of less than 1 MHz.[11] This is not necessarily high enough to use the smallest cantilevers available today. Finally, in the liquid-environment FM-AFM using the low-noise OBD sensors reported so far, a piezoactuator has been used for cantilever excitation.[11] Thus, the amplitude and phase responses to cantilever excitation have been heavily distorted, which has often prevented the stable self-oscillation and quantitative force measurements in FM-AFM.

In this study, I developed a wideband low-noise OBD sensor with a photothermal cantilever excitation system. The developed OBD sensor has a 10 MHz bandwidth and 4.7 fm/$\sqrt{\text{Hz}}$ deflection PSD in water, demonstrating the shot-noise-limited performance in liquid for the first time. Clean amplitude and phase versus frequency curves without

a)Electronic mail: fukuma@staff.kanazawa-u.ac.jp.

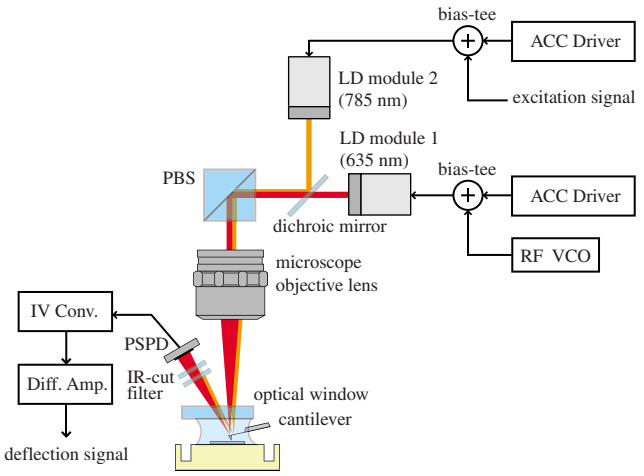

FIG. 1. (Color online) Schematic of the experimental setup for the developed OBD sensor with the photothermal cantilever excitation system.

distortion have been obtained with photothermal excitation. The wide bandwidth and the replaceable objective lenses allow the detection of the deflection of the small cantilevers (length of $\ell_c = 35\ \mu$m) with the n_{zs} value of 5.5 fm/$\sqrt{\text{Hz}}$. True atomic-resolution FM-AFM images of mica in liquid have been obtained with the developed deflection sensor using photothermal excitation.

II. BASIC PRINCIPLE AND SETUP

Figure 1 shows the overall experimental setup for the developed OBD sensor with the photothermal cantilever excitation system. In the OBD method, a focused laser beam is irradiated onto the back of the cantilever. The reflected laser beam is detected with a position-sensitive photodetector (PSPD), which is typically a four-divided silicon photodiode array. The photoinduced current at each element is converted to a voltage signal by the current-to-voltage converter (*IV* Conv.). The converted voltage signals are fed into a differential amplifier (Diff. Amp.), which outputs a signal proportional to the difference between the input signals.

As the cantilever deflects, the laser spot on the PSPD is displaced. This gives rise to the difference between the photoinduced currents at the photodiode elements. Therefore, the output from the Diff. Amp. changes in proportion to the cantilever deflection and is referred to as the "deflection signal."

III. WIDEBAND PHOTODETECTOR

The use of higher resonance frequency gives a faster time response and a better sensitivity in dynamic force microscopy.[2,3] The use of torsional resonances[17] and higher flexural modes[18] have been explored for visualizing various surface properties other than topography. The higher flexural modes are also used for oscillating a cantilever with very small amplitude.[19] The higher harmonics of the fundamental resonance have been investigated in order to understand the nonlinear cantilever dynamics[20] and enhance the spatial resolution.[21,22] These examples of recent research illustrate the growing demand for wideband cantilever deflection sensors.

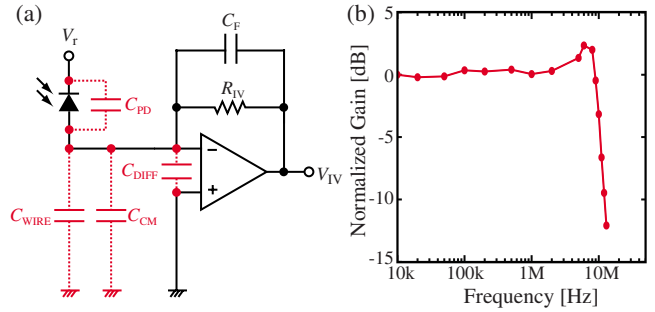

FIG. 2. (Color online) (a) Equivalent circuit of the *IV* Conv. connected to the photodiode. (b) Frequency response of the normalized gain of the *IV* Conv. ($V_r = 15$ V).

However, enhancing the bandwidth without compromising the noise performance has been a great challenge. In fact, the bandwidth of the previously reported low-noise OBD sensors has been limited to less than 1 MHz.[11] In this study, I developed a low-noise OBD sensor with a bandwidth of 10 MHz without deteriorating the noise performance. The detection bandwidth of the OBD sensor is determined by the bandwidth of the *IV* Conv. and the Diff. Amp. In this section, the detailed design and performance of these two components are described.

A. IV converter

Figure 2(a) shows the equivalent circuit of the *IV* Conv. connected to the photodiode. The *IV* Conv. consists of the feedback resistor R_{IV} and capacitor C_F, and the operational amplifier (OPAMP). The −3 dB bandwidth of the *IV* Conv. (B_{IV}) is given by

$$B_{IV} = \sqrt{\frac{\text{GBP}}{2\pi R_{IV} C_S}}, \tag{1}$$

where GBP is the gain bandwidth product (GBP) of the OPAMP and C_S is the source capacitance, that is, the total capacitance to the ground on the inverting input of the OPAMP. The capacitance is the sum of the common-mode and differential-mode input capacitances (C_{CM} and C_{DIFF}, respectively), the photodiode capacitance (C_{PD}) and the parasitic capacitance of the circuit pattern and the wiring (C_{WIRE}),

$$C_{\text{S}} = C_{\text{CM}} + C_{\text{DIFF}} + C_{\text{PD}} + C_{\text{WIRE}}. \tag{2}$$

Equations (1) and (2) show that an OPAMP with higher GBP is desirable for obtaining wider bandwidth. However, such a high-speed OPAMP tends to dissipate large power, leading to a temperature drift of the PSPD and its supporting mechanics. It is desirable to place the *IV* Conv. far from the PSPD to ensure thermal stability, while the wire connecting the PSPD and the *IV* Conv. should be minimized for a small C_{WIRE}.

One of the effective ways of reducing the power consumption is to use a power supply voltage as low as possible. Thus, a high-speed OPAMP that can be operated with a low supply voltage is desirable. In the developed OBD sensor, OPA4354 (Texas Instruments) was used with a power supply

voltage of ±2.5 V. The OPAMP typically has a GBP of 100 MHz. The output voltage of the *IV* Conv. (V_{IV}) measured with a static cantilever is given by[13]

$$V_{IV} = R_{IV}\eta\alpha\frac{P_0}{N_{\mathrm{PD}}}, \tag{3}$$

where α, η, P_0, and N_{PD} are laser power attenuation factor in the optical path from the focus lens to the PSPD, the efficiency of photocurrent conversion at the PSPD, the laser power measured underneath the focus lens, and the number of photodiode elements in the PSPD, respectively. In the present design, R_{IV}=10 kΩ, η=0.43, P_0=2 mW, and N_{PD}=4. α is 0.8 for a gold-coated cantilever and less than that for other cantilevers. From Eq. (3), V_{IV} is less than 1.72 V. The output swing of OPA4354 is ±2 V when the power supply voltage is ±2.5 V. This low power consumption of the OPAMP allows us to place it close to the PSPD without deteriorating the thermal stability.

Equations (1) and (2) show that a PSPD with small C_{PD} is desirable for a wide B_{IV}. C_{PD} depends on the reverse bias voltage V_r as well as on the material and structure of the photodiode. The application of V_r results in an expansion of the depletion layer in the photodiode and hence a reduction in C_{PD}.

In the developed OBD sensor, a four-divided Si *p-i-n* photodiode array (S6695–01: Hamamatsu Photonics) was used as the PSPD. The *p-i-n* structure of the diode and the small detection area (2×2 mm^2) provide a small C_{PD}: 3 pF at V_r=15 V. OPA4354 typically has C_{CM}=2 pF and C_{DIFF}=2 pF. The other parasitic capacitance, C_{WIRE}, is estimated to be approximately 8 pF in the present design. From Eq. (2), the total source capacitance C_S is 15 pF. B_{IV} calculated using Eq. (1) with the parameters mentioned above is 10.6 MHz. Figure 2(b) shows the frequency response of the normalized gain of the *IV* Conv. developed in this study. B_{IV}, estimated from the profile is 10 MHz, which shows good agreement with the calculated value.

The feedback capacitance C_F is necessary for suppressing the gain peak in the frequency response of the *IV* Conv. For the maximally flat second-order Butterworth frequency response, C_F should be set to

$$C_F = \sqrt{\frac{C_S}{\pi R_{IV}\mathrm{GBP}}}. \tag{4}$$

On the basis of Eq. (4) and the parameters described above, C_F should be set to 2.2 pF in the developed OBD sensor. In the actual *IV* Conv., C_F was set to 2.0 pF, taking the stray capacitance into account. The profile in Fig. 2(b) shows a small peak at around 8 MHz. This is because either the actual C_S is larger than 15 pF or C_F is smaller than 2.2 pF.

B. Differential amplifier

Figure 3(a) shows the simplified circuit of the developed Diff. Amp. Note that the input, output, and summing stages, and the power supply lines with the decoupling capacitors are omitted. The current signals from the four photodiode elements are converted to the voltage signals at the *IV* Conv.

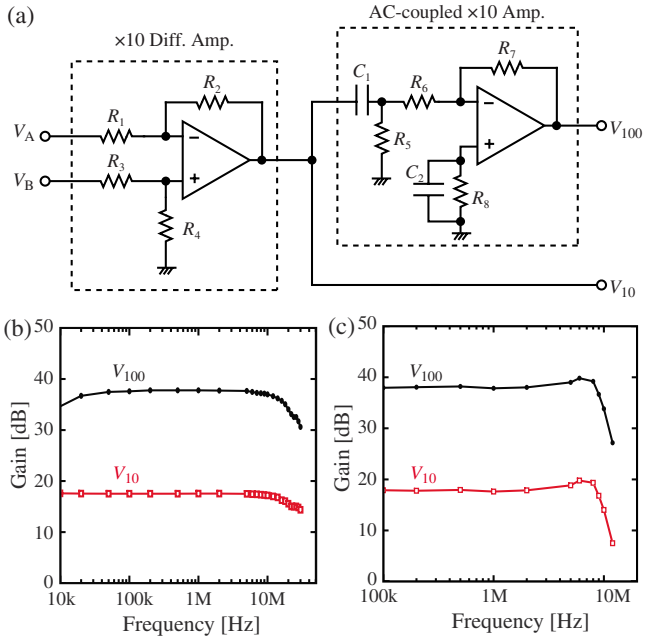

FIG. 3. (Color online) (a) Simplified circuit of the Diff. Amp. The input, output, and summing stages, and the power supply lines with the decoupling capacitors are omitted. (b) Frequency response of the gain of the Diff. Amp. (c) Frequency response of the gain of the Diff. Amp. multiplied by the normalized gain of the *IV* Conv. shown in Fig. 2(b).

The four voltage signals output from the *IV* Conv. are fed into the Diff. Amp. At the input stage of the Diff. Amp., the voltage signals from the upper and lower two elements are respectively summed to generate two voltage signals (V_A and V_B). These two signals are input to the ×10 Diff. Amp. stage which outputs the difference between V_A and V_B (V_{10}). While V_{10} is output from the Diff. Amp. as the ×10 deflection signal, it is also routed to the ac-coupled ×10 Amp. stage to produce the ×100 deflection signal (V_{100}).

The deflection sensitivity S_z of the OBD sensor is given by[13]

$$S_z = 6\chi\eta\alpha n_m R_{IV} A_{\mathrm{diff}}\frac{P_0\ell_f}{a_0\ell_c}. \tag{5}$$

χ is the correction factor for the Gaussian laser beam, n_m is the refraction index for the medium of the operating environment, A_{diff} is the gain of the Diff. Amp., ℓ_f is the focal length of the focus lens, and ℓ_c is the cantilever length. In the present design, A_{diff} is 17.5 dB (×7.5) for V_{10} and 37.5 dB (×75) for V_{100} because of the −2.5 dB gain of the input stage. The values for the other parameters are χ=1.13, ℓ_f=40 mm, a_0=1.1 mm, and ℓ_c=125 μm. In air (n_m=1.0), V_{10} is mainly used and S_z for V_{10} is 102 mV/nm. In liquid (n_m=1.33 for water), V_{100} is mainly used and S_z for V_{100} is 1.35 V/nm.

The cantilever oscillation amplitude (A) is typically 1–20 nm in air while that in liquid is 0.1–2 nm. The large amplitude in air is necessary for preventing the tip adhesion caused by the large electrostatic and van der Waals forces. These long-range attractive forces are greatly reduced in liquid, making it possible to oscillate the cantilever with small amplitude. The small-amplitude operation is proven to be

effective for enhancing the sensitivity to the short-range interaction force,[23] thereby obtaining high spatial resolution.[24]

For a reasonable immunity to the electronic circuit noise, the amplitude of the deflection signal should be larger than 100 mV, while the amplitude should be kept lower than a few volts to avoid the harmonic distortions caused by the insufficient slew rate of the OPAMP at high frequencies. Thus, it is very difficult to cover the amplitude range from 0.1 to 20 nm with a single deflection output. In the present design, two deflection outputs with different gains are used; V_{10} and V_{100}. V_{10} output is mainly used for applications in air in both dynamic and static modes while the ac-coupled V_{100} output is mainly used for applications in liquid only in the dynamic mode.

The $\times 10$ Diff. Amp. stage typically consists of four resistors and an OPAMP. The circuit can be implemented by a single-chip instrumentation amplifier with integrated resistors. This eliminates the need for precise matching of the four resistor values for a high common-mode rejection ratio (CMRR). The high CMRR is important for suppressing the common-mode noise arising from the laser power fluctuation. However, commercially available low-noise instrumentation amplifiers are not fast enough to constitute the $\times 10$ Diff. Amp. with a bandwidth higher than 10 MHz. Thus, in this study, a high-speed OPAMP, OPA820 (Texas Instruments), and four well-matched external resistors are used to construct the Diff. Amp. stage.

The Diff. Amp. should have a wide bandwidth as well as a high dc stability for operating the AFM in both dynamic and static modes. Low input voltage noise in the frequency range from dc to a few tens of megahertz is required. Although current feedback OPAMPs are faster than those with voltage feedback, they generally have large input current noise and bias offset current. Reducing the resistor values could partially compensate such effects but increase the power consumption and hence deteriorate thermal stability. Moreover, a high-speed OPAMP generally dissipates large power, which can deteriorate the dc stability of the circuit.

OPA820 is a voltage feedback amplifier having a high dc precision and stability. The GBP of OPA820 is typically 280 MHz, which is high enough for obtaining a bandwidth over 10 MHz. The input voltage noise density is less than 2.5 $\mathrm{nV}/\sqrt{\mathrm{Hz}}$ for a frequency higher than 100 kHz and less than 15 $\mathrm{nV}/\sqrt{\mathrm{Hz}}$ even at 10 Hz. The OPAMP is operated with a ± 5 V power supply voltage, giving a ± 4 V output swing. From the S_z values described above, the amplitude ranges in air and water corresponding to 0.1–4 V are $V_{10}=1-40$ nm and $V_{100}=0.074-3$ nm, respectively. These ranges cover the typical amplitude ranges used in air and liquid.

Figure 3(b) shows the frequency response of the gain of the developed Diff. Amp. The profiles show the -3 dB bandwidth of the Diff. Amp. (B_{DIFF}) is 30 MHz for V_{10} and 20 MHz for V_{100}. The decrease in the V_{100} gain in the low-frequency range reflects the influence of ac coupling with an 8 kHz cutoff frequency. The frequency response of the total gain of the preamplifier (i.e., *IV* Conv. and Diff. Amp.) is plotted in Fig. 3(c). The profiles show that the -3 dB bandwidth of the deflection sensor is about 10 MHz for both outputs.

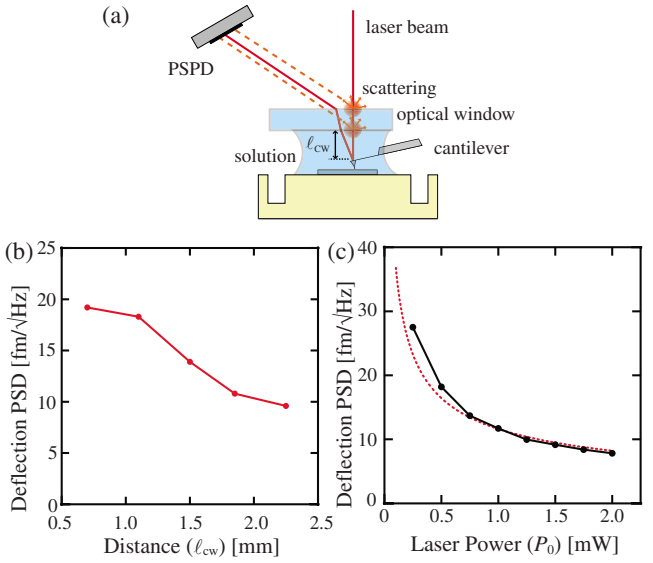

FIG. 4. (Color online) (a) Schematic of the OBD sensor showing the laser beam interference at the PSPD surface caused by scattering at the air/glass and glass/liquid interfaces. (b) ℓ_{cw} dependence of n_{zs}. (c) P_0 dependence of n_{zs}.

IV. SHOT-NOISE-LIMITED NOISE PERFORMANCE

The noise performance of the OBD sensor is ultimately limited by the photodiode shot noise. The deflection PSD arising from the photodiode shot noise (n_{zp}) is given by[13]

$$n_{zp}=\frac{a_0\ell_c}{6\chi n_m\ell_f}\sqrt{\frac{2e}{\eta\alpha P_0}}. \tag{6}$$

However, the noise performance of the actual OBD sensor is often limited by other noise sources such as laser mode hopping and interference, Johnson noise at R_{IV}, and other electronics noise. Thus, the reduction in such noise to attain the shot-noise-limited noise performance is essential for developing the low-noise OBD sensor.

In previous reports,[11,13] the shot-noise-limited noise performance was obtained only in air, while the performance in liquid has been limited by other factors. In this section, what limits the noise performance in liquid is described and a way of achieving the shot-noise-limited performance even in liquid is presented.

A. Optical window

The major difference between the OBD sensors in air and that in liquid is the existence of the air/glass and glass/liquid interfaces in the optical path of the laser beam, as shown in Fig. 4(a). The reflection and scattering at the interfaces can lead to a large increase in deflection noise. Some of the reflected laser beam returns to the laser diode and induces laser mode hopping, which is referred to as optical feedback noise. Some of the scattered laser beam is directed to the PSPD and interferes with the laser beam reflected at the back of the cantilever. This also increases the deflection noise and is referred to as optical interference noise.

In the previous report,[11] the laser power modulation with a rf signal (300–500 MHz) was employed to reduce the optical noise. The rf modulation changes the laser oscillation mode from single mode to multimode. Since mode hopping originates from the competition between the possible laser oscillation modes, the multimode laser inherently has less mode hopping than the single-mode laser. Therefore, the optical feedback noise is greatly reduced. Moreover, the multimode laser has a shorter coherence length (ℓ_{ch}) and, hence, the interference at the PSPD surface is also reduced by rf modulation.

Although rf modulation is effective, it cannot completely eliminate optical noise. Thus, it is important to prevent that the laser beam partially returns to the laser diode or is directed to the PSPD. In the present design, I introduced the antireflection (AR)-coated optical window for reducing the laser reflection and scattering at the interfaces. The distance from the back of the cantilever to the optical window (ℓ_{cw}) is also an important factor. The difference in the optical path length between the laser beams scattered at one of the interfaces and reflected at the back of the cantilever ($\Delta\ell$) increases with increasing ℓ_{cw}, as shown in Fig. 4(a). In order to prevent the laser beam interference at the PSPD surface, $\Delta\ell$ should be longer than ℓ_{ch}.

Figure 4(b) shows the ℓ_{cw} dependence of n_{zs} measured in water. The result shows that n_{zs} decreases by 50% with increasing ℓ_{cw} from 0.7 to 2.3 mm. From Fig. 4(a), $\Delta\ell$ is approximately $2\ell_{cw}$ (or $2\ell_{cw}+t_{ow}$) for scattering at the glass/water (or air/glass) interface. t_{ow} is the thickness of the optical window and is 2 mm in the present design. Since n_{zs} decreases with increasing ℓ_{cw} up to ~2 mm, ℓ_{ch} of the rf-modulated laser beam used in this experiment should be approximately 4–6 mm.

Figure 4(c) shows the P_0 dependence of n_{zs} measured in water. The experimentally measured values (solid line) show good agreement with the values theoretically calculated with Eq. (6) (dotted line). This demonstrates that n_{zs} of the developed sensor is predominantly limited by the photodiode shot noise, even in liquid. The results show that the shot-noise-limited noise performance can be achieved by employing rf laser power modulation and placing the AR-coated optical window sufficiently far from the cantilever.

B. Small cantilevers

In order to detect the deflection of small cantilevers with low n_{zs}, the laser spot size at the back of the cantilever should be small enough to prevent the severe reduction in α owing to laser power loss. For a small laser spot size, the focus lens should have a large numerical aperture (NA). Such a high-NA lens generally has a short ℓ_f, leading to a large n_{zs} [Eq. (6)]. Therefore, the optimum focus lens differs for cantilevers with different dimensions.

In the previous report,[13] replaceable microscope objective lenses were introduced to satisfy the above requirements. The ×5 objective lens with ℓ_f=40 mm was used for long cantilevers, while the ×20 objective lens with ℓ_f =10 mm was used for short cantilevers. However, n_{zs} measured with the ×5 objective lens showed lower n_{zs} values than those obtained with the ×20 objective lens, even with the smallest cantilever used in the experiment, and the merit of using replaceable objective lenses could not be proven.

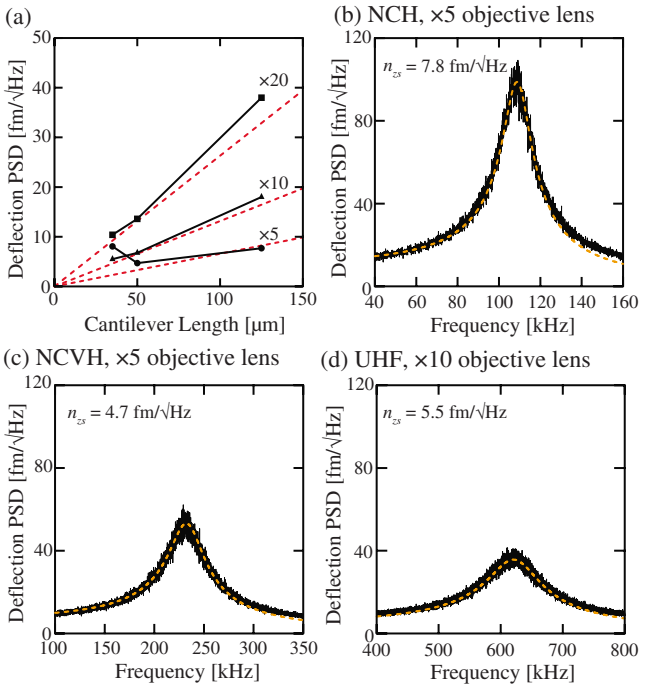

FIG. 5. (Color online) (a) ℓ_c dependence of n_{zs} measured with the ×5, ×10, and ×20 objective lenses. The solid lines show the experimentally measured values while the dotted lines show the theoretically calculated values using Eq. (6). ℓ_f=10, 20, and 40 mm for ×20, ×10, and ×5 objective lenses, respectively. [(b)–(d)] The solid lines show the experimentally measured deflection PSD with different cantilevers in water while the dotted lines show the thermally induced deflection PSD calculated using Eq. (7). (b) NCH cantilever (ℓ_c=125 μm), ×5 objective lens. (c) NCVH cantilever (ℓ_c=50 μm), ×5 objective lens. (d) UHF cantilever (ℓ_c=35 μm), ×10 objective lens.

In the present design, I introduced a ×10 objective lens with ℓ_f=10 mm in addition to the ×5 and ×20 lenses. The n_{zs} values measured with these three lenses in water are shown in Fig. 5(a). Three types of cantilevers with different ℓ_c were used: NCH (ℓ_c=125 μm), NCVH (ℓ_c=50 μm), and UHF (ℓ_c=35 μm). The solid lines show experimentally measured values while the dotted lines show the theoretically calculated values using Eq. (6).

The experimentally measured values (solid lines) show good agreement with the calculated values (dotted lines), except for the value measured with the UHF cantilever and the ×5 objective lens. This deviation is due to the excess laser spot size (about 30 μm in diameter) compared with the cantilever dimensions. The ×5 lens gives the lowest n_{zs} values (7.8 and 4.7 fm/$\sqrt{\text{Hz}}$, respectively) for the NCH and NCVH cantilevers. For the UHF cantilever, the ×10 lens gives the lowest n_{zs} value (5.5 fm/$\sqrt{\text{Hz}}$). The ×20 lens yields the largest n_{zs} values for all the cantilevers used in this experiment. However, the good agreement between the experimental values and the theoretical calculation suggests that the ×20 lens should give rise to the best performance for cantilevers shorter than 10 μm.

The deflection PSD spectra measured under the best conditions for the three cantilever types are shown in Figs. 5(b)–5(d), respectively. The experimentally measured spectra

(solid lines) show good agreement with the values calculated (dotted lines) using the following equation for the PSD of the cantilever thermal Brownian motion (n_{zB}):

$$n_{zB} = \sqrt{\frac{2k_BT}{\pi f_0 kQ}\frac{1}{[1-(f/f_0)^2]^2+[f/(f_0Q)]^2}}, \quad (7)$$

where k_B, T, Q, and k are Boltzmann's constant, absolute temperature, Q factor, and spring constant of the cantilever, respectively. The results show that the influence of n_{zs} on the deflection PSD is negligible compared with that of n_{zB} for all the cantilever dimensions. Thus, the deflection sensor provides the maximum performance such that it is limited only by the thermal cantilever vibration in dynamic-mode AFM.

V. PHOTOTHERMAL EXCITATION

In applications in air or vacuum, it is common to use a piezoactuator to excite the cantilever vibration. However, in the case of liquid environments, the amplitude and phase versus frequency curves obtained with piezoexcitation are heavily distorted by the acoustic resonances of the liquid cell.[11] This problem is particularly serious in FM-AFM. The distortion often prevents stable self-oscillation of the cantilever, particularly during coarse approach of the tip. It also hinders quantitative measurements of the conservative and dissipative forces in FM-AFM.

In order to solve these problems, other cantilever excitation methods have been proposed. Among the most common is the magnetic excitation method.[25] In this method, a cantilever with a magnetic bead or a thin film is excited with an ac magnetic field generated by the coil under or above the cantilever. The method eliminates the spurious resonances in the phase and amplitude curves. However, the magnetic materials, typically containing transient metals such as Co or Ni, are not necessarily passive in typical solutions used in AFM experiments or biological research and hence may produce ionic contaminations.[26,27] Attaching a magnetic bead on the back of the cantilever is becoming more and more difficult as the cantilever dimensions are reduced. Driving the coil at high frequency requires high driving voltage and also produces large heat dissipation. Thus, it is highly difficult to drive a stiff ($k>20$ N/m) cantilever at a frequency higher than 1 MHz by magnetic excitation.

Another method of avoiding distortions in the amplitude and phase curves is photothermal excitation.[28] In this method, a laser beam with modulated power is irradiated onto the thin gold film on the back of the cantilever. Because of the thermal expansion of the Si cantilever and the gold film, cantilever oscillation synchronized with the laser power modulation is induced. The gold film is stable in most of the solutions used in AFM experiments. In addition, the gold coating enhances the reflectivity of the back of the cantilever. It is easy to drive a stiff cantilever at a frequency higher than 10 MHz by photothermal excitation owing to the fast time response of the laser power to the driving current.

In the present design, I employed photothermal excitation for a better applicability to small cantilevers with high resonance frequencies. The major difficulty in the design was the addition of optical components without deteriorating the low-noise characteristics. In this section, the design guideline for resolving this issue is described.

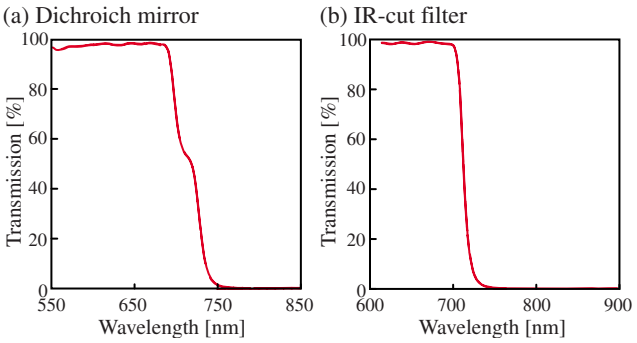

FIG. 6. (Color online) The transmission spectra of (a) the dichroic mirror and (b) the IR-cut filter.

A. Filter and mirror

The experimental setup for photothermal excitation is shown in Fig. 1. In this design, the 635 nm red laser beam is used for detecting the cantilever deflection. In order to separate the excitation laser beam from the detection laser beam, an infrared (IR) laser beam with the wavelength of 785 nm was used. The red and IR laser diodes are driven by the automatic current constant (ACC) driver with a power modulation function. The power of the red laser is modulated at 300 MHz to reduce the laser coherence,[11] while that of the IR laser is modulated at the cantilever resonance frequency.

The red and IR laser beams are directed to the dichroic mirror with an incident angle of 45°. At the dichroic mirror, the IR laser beam is reflected and the red laser beam is transmitted, as shown in Fig. 1. The transmission spectrum of the dichroic mirror is shown in Fig. 6(a). The two laser beams are reflected by the polarizing beam splitter and focused with the objective lens. While the red laser beam is focused on the free end of the cantilever for the best deflection sensitivity, the IR laser beam is focused on the fixed end of the cantilever to provide the best excitation efficiency.[29]

The reflected laser beams are directed to the double IR-cut filters. The red laser beam passes through the filter while the IR laser beam is blocked by the filter, as shown in Fig. 6(b). Note that Fig. 6(b) shows the transmission characteristics for the "single" IR-cut filter. The selectivity of the single filter is high enough for the applications in air ($A>1$ nm), even with a stiff cantilever ($k>20$ N/m), because of the high Q factor. For liquid environments, soft cantilevers should be used ($k<20$ N/m) if the single IR-cut filter is used. In order to use a stiff cantilever ($k>20$ N/m) in liquid, I used two IR-cut filters in series, as shown in Fig. 1. This configuration provides sufficient selectivity even with stiff cantilevers in liquid.

B. Amplitude and phase curves

Figure 7(a) shows the amplitude versus frequency curve measured with photothermal excitation. The deflection PSD measured without cantilever excitation is also displayed in the same figure. The thermal PSD spectrum shows good

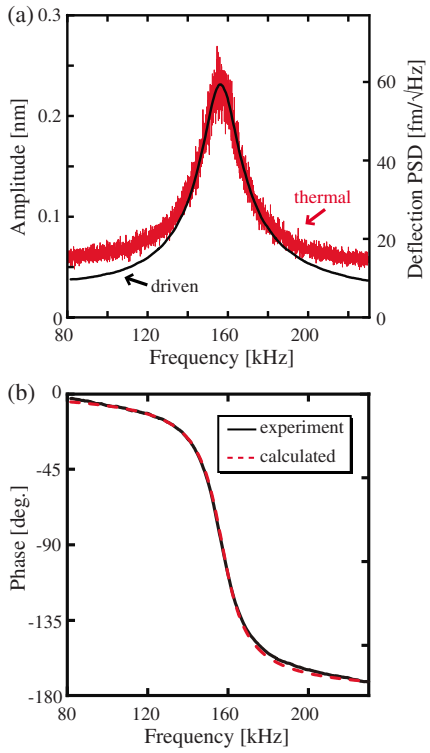

FIG. 7. (Color online) (a) Amplitude and (b) phase vs frequency curves measured with photothermal excitation in water. The deflection PSD spectrum measured without cantilever excitation is superposed on the driven amplitude curve in (a). Q and f_0 obtained by fitting the thermal PSD spectrum with Eq. (8) are 8.7 and 157.079 kHz, respectively. The dotted line in (b) is calculated with these parameters in Eq. (9), while the solid line shows the experimentally measured values.

agreement with the driven amplitude curve around f_0. The slight deviation of the driven amplitude curve from the thermal spectrum is due to the influence of n_{zs}. Including this influence, the overall deflection PSD (n_z) is given by

$$n_z = \sqrt{n_{zs}^2 + n_{zB}^2}. \tag{8}$$

By fitting the thermal spectrum with this equation and Eq. (7), $Q=8.7$ and $f_0=157.079$ kHz are obtained

Figure 7(b) shows the phase versus frequency curve measured with photothermal excitation. The phase versus frequency curve of a driven cantilever is given by

$$\phi(f) = \tan^{-1}\left\{\frac{1}{Q(f_0/f - f/f_0)}\right\}. \tag{9}$$

With this equation and the Q and f_0 values obtained from the thermal spectrum, the theoretically expected phase curve is calculated, as indicated by the dotted line in Fig. 7(b). The calculated phase curve shows excellent agreement with the experimental result indicated by the solid line. The results show that the developed photothermal excitation system is capable of driving a cantilever without exciting spurious resonances. This enables accurate quantitative force measurements as well as stable FM-AFM imaging.

C. Thermal stability

Figure 8(a) shows the laser power dependence of the cantilever oscillation amplitude induced by photothermal excitation. The excitation laser has the maximum power rating

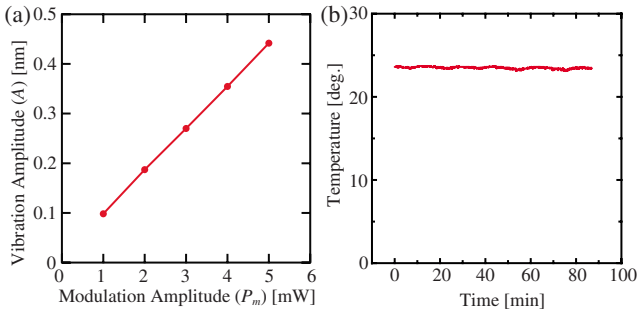

FIG. 8. (Color online) (a) P_m dependence of A induced by photothermal excitation. (b) The temperature variation of water (150 $\mu\ell$) in the liquid cell. The excitation laser was turned on at time $t=0$. The cantilever used was NCH (Nanoworld) with a Au/Ti coating ($k=27$ N/m, $Q=8.7$).

of 20 mW. The average laser power P_0 was set at 5 mW and the laser power modulation amplitude P_m was varied from 1 to 5 mW. The cantilever oscillation amplitude A shows a linear dependence on P_m. The maximum value of A at $P_0=5$ mW was 0.44 nm in this particular experiment. This excitation efficiency is sufficient for the small-amplitude operation of FM-AFM, where A is usually set at 0.1–0.3 nm. This result demonstrates that the developed photothermal excitation system is compatible with stiff cantilevers ($k>20$ N/m) in liquid.

The average laser power of 5 mW is relatively high. Thus, we examined whether the laser beam irradiation could increase the liquid temperature. Figure 8(b) shows the temperature variation of the water (150 $\mu\ell$) in the liquid cell measured with photothermal excitation turned on ($P_0=5$ mW and $P_m=5$ mW). The temperature was measured using a thermocouple sensor with a small sensor head. The sensor head is coated with a Teflon thin film and immersed in the liquid. The laser was turned on at $t=0$ on the x-axis. However, no significant temperature variation was observed during the measurement period (up to $t=90$ min). The result shows that the heating effect of the IR laser beam is negligible for most applications.

We measured the reflected and transmitted laser beam power by irradiating the IR laser beam at the midpoint of the cantilever and obtained 80% and 10% for the reflection and transmission coefficients, respectively. The rest of the power (10%) is expected to be dissipated at the back of the cantilever and rapidly diffused to the cantilever support metal. Thus, if any heating effect exists, it should be due to the 10% transmitted beam. In the actual experiment, the IR laser beam is irradiated at the fixed end of the cantilever so that the transmission coefficient is further decreased. This accounts for the observed small heating effect of the IR laser beam.

VI. ATOMIC-RESOLUTION IMAGING

The developed OBD sensor was integrated into the FM-AFM instrument reported previously.[13] Figure 9 shows the FM-AFM image of mica taken in a phosphate buffer saline solution using the developed system. The tip-sample distance was regulated in the constant frequency-shift mode using the Nanonis SPM controller (RC-4). A high-voltage amplifier (ENP-4014B: Echo Electronics) was used to drive the

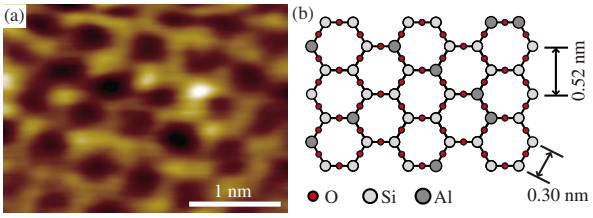

FIG. 9. (Color online) (a) FM-AFM image of mica in phosphate buffer solution ($\Delta f = +500$ Hz, $A = 0.098$ nm, tip velocity: 117 nm/s). The cantilever used was NCH (Nanoworld) with a Au/Ti coating ($k = 19.4$ N/m, $f_0 = 104.4$ kHz). The cantilever vibration was excited with the developed photothermal excitation system. (b) Atomic-scale model of the cleaved mica surface.

custom-built piezotube scanner. A Si cantilever (NCH: Nanoworld) was driven in the constant-amplitude mode using the developed photothermal excitation system and the digital phase-locked loop (PLL) system (OC-4: Nanonis). The PLL was also used for frequency-shift detection.

The image shows the honeycomblike pattern characteristic of the cleaved mica surface [Fig. 9(b)]. Atomic-scale bright spots are observed on some of the honeycomb patterns. In the previous report,[12] these bright spots were tentatively attributed to the aluminum ions constituting the aluminosilicate mesh of the mica surface. The result demonstrates the applicability of the developed OBD sensor to true atomic-resolution imaging in liquid.

ACKNOWLEDGMENTS

This research was supported by PRESTO, Japan Science and Technology Agency.

[1] G. Binnig, C. F. Quate, and C. Gerber, Phys. Rev. Lett. **56**, 930 (1986).
[2] T. R. Albrecht, P. Grütter, D. Horne, and D. Ruger, J. Appl. Phys. **69**, 668 (1991).
[3] Y. Martin, C. C. Williams, and H. K. Wickramasinghe, J. Appl. Phys. **61**, 4723 (1987).
[4] G. M. McClelland, R. Erlandsson, and S. Chiang, *Review of Progress in Quantitative Non-Destructive Evaluation* (Plenum, New York, 1988), Vol. 6B, pp. 1307–1314.
[5] G. Meyer and N. M. Am, Appl. Phys. Lett. **53**, 1045 (1988).
[6] C. Schönenberger and S. F. Alvarado, Rev. Sci. Instrum. **60**, 3131 (1989).
[7] G. Neubauer, S. R. Cohen, G. M. McClelland, D. Horne, and C. M. Mate, Rev. Sci. Instrum. **61**, 2296 (1990).
[8] M. Tortonese, H. Yamada, R. C. Barrett, and C. F. Quate, *The Proceedings of Transducers*, 1991, Publication No. 91 CH2817–5 (IEEE, Pennington, NJ, 1991), pp. 448–451.
[9] T. Itoh and T. Suga, Nanotechnology **4**, 218 (1993).
[10] F. J. Giessibl, *Noncontact Atomic Force Microscopy (Nanoscience and Technology)* (Springer, Berlin, 2002), Chap. 2.
[11] T. Fukuma, M. Kimura, K. Kobayashi, K. Matsushige, and H. Yamada, Rev. Sci. Instrum. **76**, 053704 (2005).
[12] T. Fukuma, K. Kobayashi, K. Matsushige, and H. Yamada, Appl. Phys. Lett. **87**, 034101 (2005).
[13] T. Fukuma and S. P. Jarvis, Rev. Sci. Instrum. **77**, 043701 (2006).
[14] T. Fukuma, M. J. Higgins, and S. P. Jarvis, Biophys. J. **92**, 3603 (2007).
[15] T. Fukuma, M. J. Higgins, and S. P. Jarvis, Phys. Rev. Lett. **98**, 106101 (2007).
[16] T. Fukuma, A. S. Mostaert, and S. P. Jarvis, Nanotechnology **19**, 384010 (2008).
[17] M. Reinstädtler, T. Kasai, U. Rabe, B. Bhushan, and W. Arnold, J. Phys. D **38**, R269 (2005).
[18] N. F. Martinez, S. Patil, J. R. Lozano, and R. Garcia, Appl. Phys. Lett. **89**, 153115 (2006).
[19] S. Kawai, S. Kitamura, D. Kobayashi, S. Meguro, and H. Kawakatsu, Appl. Phys. Lett. **86**, 193107 (2005).
[20] A. Raman, J. Melcher, and R. Tung, Nanotoday **3**, 20 (2008).
[21] S. Hembacher, F. J. Giessibl, and J. Mannhart, Science **305**, 380 (2004).
[22] J. Preiner, J. Tang, V. Pastushenko, and P. Hinterdorfer, Phys. Rev. Lett. **99**, 046102 (2007).
[23] F. J. Giessibl, H. Bielefeldt, S. Hembacher, and J. Mannhart, Appl. Surf. Sci. **140**, 352 (1999).
[24] F. J. Giessibl, S. Hembacher, H. Bielefeldt, and J. Mannhart, Science **289**, 422 (2000).
[25] S. P. Jarvis, A. Oral, T. P. Weihs, and J. B. Pethica, Rev. Sci. Instrum. **64**, 3515 (1993).
[26] I. Revenko and R. Proksch, J. Appl. Phys. **87**, 526 (2000).
[27] B. Rogers, D. York, N. Whisman, M. Jones, K. Murray, and J. D. Adams, Rev. Sci. Instrum. **73**, 3242 (2002).
[28] N. Umeda, S. Ishizaki, and H. Uwai, J. Vac. Sci. Technol. B **9**, 1318 (1991).
[29] D. Ramos, J. Tamayo, J. Mertens, and M. Calleja, Appl. Phys. Lett. **99**, 124904 (2006).